Multishot Diffusion-Weighted FSE Using PROPELLER MRI

James G. Pipe,[1*] Victoria G. Farthing,[1] and Kirsten P. Forbes[2]

A method for obtaining diffusion-weighted images that are free from the artifacts associated with echo-planar acquisitions, such as signal pile-up and geometric warping, is introduced. It uses an ungated, multishot fast spin-echo (FSE) acquisition that is self-navigated. The phase of the refocusing pulses is alternated to minimize non-Carr-Purcell-Meiboom-Gill (CPMG) artifacts. Several reconstruction methods are combined to make this method robust against motion artifacts. Examples are shown of clinical diffusion-weighted imaging and high-resolution diffusion tensor imaging. Magn Reson Med 47:42–52, 2002. © 2002 Wiley-Liss, Inc.
Key words: diffusion; stroke; fast spin-echo; tensor

The clinical utility of diffusion-weighted imaging (DWI) is well established and extensions of this method to measure and exploit diffusion anisotropy are very exciting. Most DWI data are collected using single-shot EPI imaging, due to extreme variability in phase between applications of diffusion gradients. This can create significant motion artifacts in multiple-shot techniques in the presence of even minor, nonrepeatable motion. However, single-shot EPI methods suffer from severe warping artifact in the presence of magnetic field inhomogeneities and the significant T_2^* decay that can occur during long echo trains makes high-resolution acquisitions challenging.

Multiple-shot fast spin-echo (FSE) methods for DWI have far less B_0-related artifacts (e.g., from metal, sinuses, and eddy currents) and can be implemented with less intensive gradient requirements than those of single-shot EPI DWI. Despite this promise, multishot FSE DWI faces two major challenges. First, the extremely high phase-sensitivity to motion requires some sort of navigator information to remove this phase prior to combination of data over multiple diffusion weightings (1–4). An alternative to this is the use of radial sampling (5), which is immune to some types of motion artifact and tends to express the remaining artifacts in a more benign way. The second challenge to multishot FSE is that the signal will not in general meet the Carr-Purcell-Meiboom-Gill (CPMG) condition, leading to unstable echoes. Norris et al. (6) introduced a method to solve the CPMG problem which was further investigated by Schick (7) and Alsop (8), but this results in a significant loss in signal. Mori and van Zijl (9) discussed the use of two navigator echoes to correct for motion-related phase effects between odd and even echoes. Other solutions to the CPMG problem have been discussed in the literature (10,11) and recently investi-

gated by Le Roux and Bastin (12,13). The latter work cycles the phase of the refocusing pulses in a quadratic manner, which mitigates non-CPMG losses in the signal, as first suggested by Murdoch (14).

The proposed work is based on the PROPELLER (Periodically Rotated Overlapping ParallEL Lines with Enhanced Reconstruction) method (15), which has inherent 2D navigator information in each FSE echo train. The proposed work builds on much of the work cited above in the following ways. First, it uses FSE data collection, which provides far greater immunity against geometric distortion than that obtained with EPI sequences. Second, it mitigates signal instability present in all diffusion-weighted FSE methods by varying the phase of the refocusing pulses using a scheme previously reported (10,11). The method of Norris cited above for addressing the CPMG problem could also be used, but the resulting signal loss proves to be a significant penalty. Third, the proposed work uses navigator information to correct data between shots, although this navigator information is not collected in a separate acquisition, as in previous schemes, and a more complete data correction is proposed. Fourth, the sequence is radial in nature, and thus uncorrected errors are expressed in a rather benign fashion, similar to earlier projection reconstruction methods.

METHOD

The proposed sequence has four main features, discussed below. They are 1) PROPELLER data collection, 2) mixed-CPMG FSE phase cycling, 3) image-space phase correction, and 4) correlation weighting.

PROPELLER Data Collection

The pulse sequence used for data collection is shown in Fig. 1. It is essentially a conventional FSE sequence with the following modifications. First, diffusion-sensitization gradients are added to either side of the first refocusing pulse. Second, the refocusing lobes for the slice and frequency encode gradients are put adjacent to the excitation and first echo gradients, respectively, to minimize cross-terms in the diffusion weighting. Third, the phase of the refocusing pulses is cycled between the x and y axes in the rotating frame. Finally, each TR the frequency and phase encode gradients are rotated about the slice selection axis as described previously (15). The resulting k-space coverage for data acquisition is illustrated in Fig. 2. Each TR, the collected echoes are phase-encoded to form a sufficiently sampled data strip (i.e., that meets the Nyquist sampling criterion), or blade, which goes through the center of k-space. The width of the blade in k-space is equal to the echo train length (ETL) divided by the field of view (FOV). In subsequent TRs this blade is rotated, so that together the

[1]MRI Department, Barrow Neurological Institute, Phoenix, Arizona.
[2]Division of Neuroradiology, Barrow Neurological Institute, Phoenix, Arizona.
*Correspondence to: Jim Pipe, Ph.D., MRI Department, Barrow Neurological Institute, 350 W. Thomas Road, Phoenix, AZ 85013.

FIG. 1. Illustration of pulse sequence used for this work (not to scale), including (from top to bottom) RF, slice gradient, diffusion-sensitizing gradient, frequency-encoding gradient, and phase-encoding gradient. The shaded areas indicate crushers common to all FSE sequences. G_f and G_p rotate about the axis normal to the slice plane between each TR.
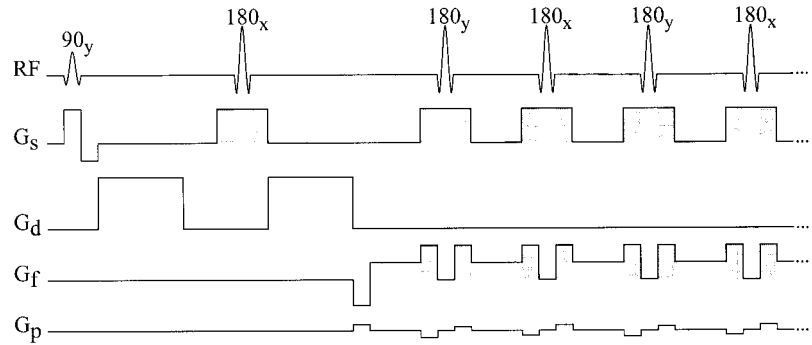
blades measure a circular region of k-space formed by their union, and separately they all measure a smaller, circular region in the center of k-space formed by their intersection. The basic idea of PROPELLER is that this oversampled region in the center of k-space can be compared between blades to correct for inconsistencies prior to combining the data. For diffusion applications, the primary inconsistency will be image-space phase differences, as discussed below. After data correction, the blades are weighted to correct for sampling density as well as uncorrected error, then gridded onto a Cartesian array, and Fourier-transformed to form the image.

Mixed-CPMG FSE Phase Cycling

At the end of the diffusion gradient application, spins are left with a spatially varying and unknown phase. Robust FSE imaging typically requires that they lie along the axis of the refocusing RF pulse, comprising the so-called CPMG condition. This condition, which greatly reduces sensitivity to inhomogeneities in B_1, is now not met in general.

Figure 3a illustrates what happens to the echo magnitude as a function of initial starting phase. Figure 3(b) illustrates the echo phase as a function of initial starting phase for the first 16 echoes. A special challenge to diffusion-weighted
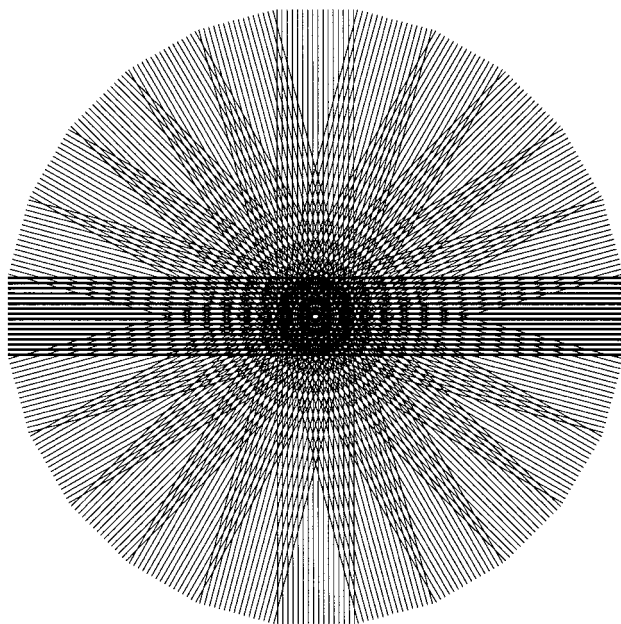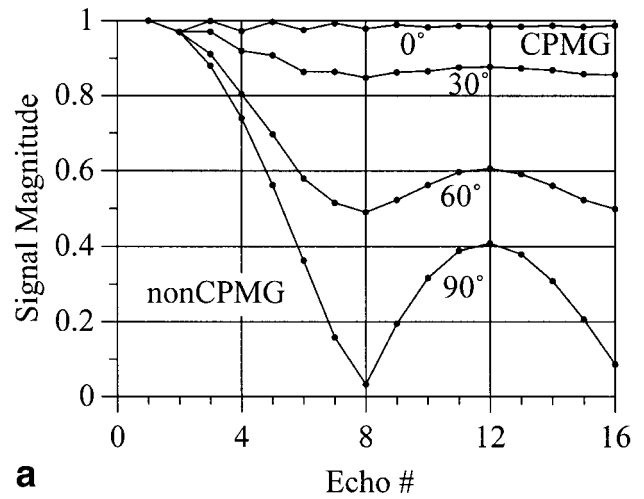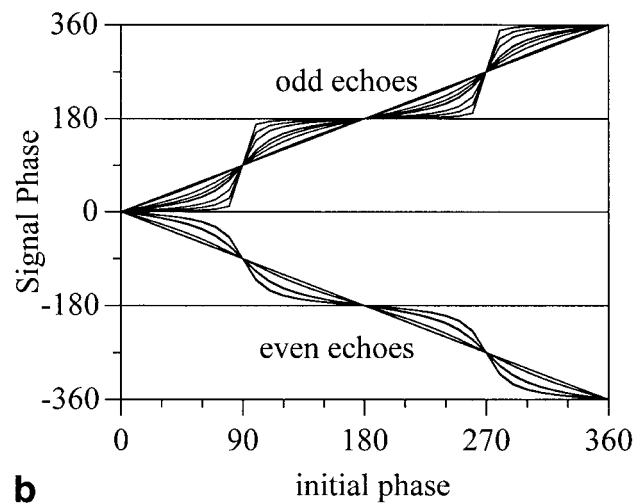
a

b

FIG. 3. The simulated magnitude (**a**) of echoes from a train of 160° refocusing pulses with a relative phase 0°, plotted for starting initial signal phases of 0° (the CPMG condition), 30°, 60°, and 90° (nonCPMG condition). The phase from these 16 echoes are overlaid (**b**) as a function of the initial starting phase. With initial phases other than 0° and 180°, the signal phase oscillates between echoes to some degree, depending on the initial spin phase.

FIG. 2. Example k-space sampling trajectory for PROPELLER MRI. The bold lines indicate the measured area of k-space (called a 'blade') by one echo train in an FSE experiment. In subsequent TRs, the blade is rotated in order to measure the remaining parts of k-space while resampling the center of k-space each time.
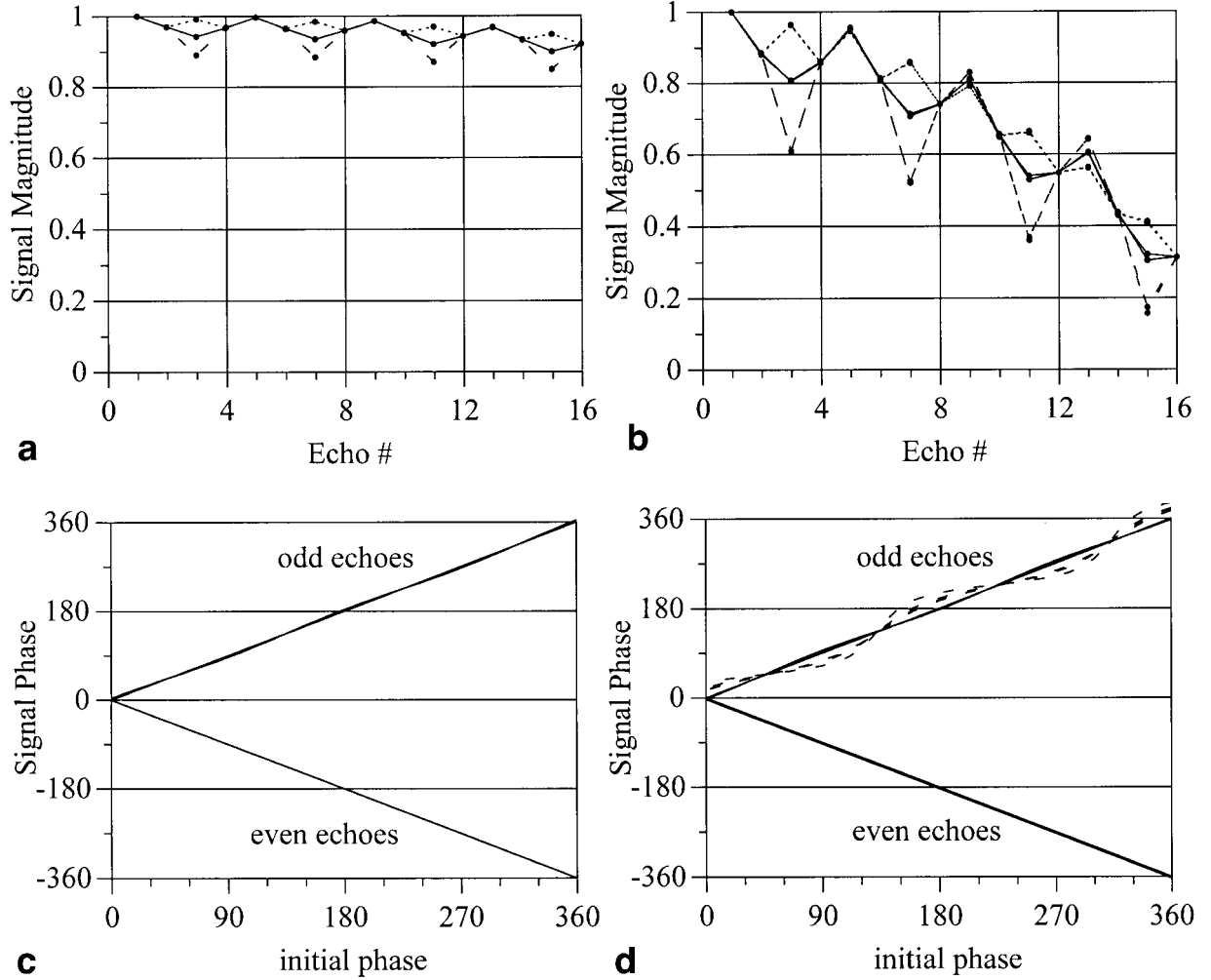
FIG. 4. The simulated magnitude of echoes from a train of 160° (**a**) and 140° (**b**) refocusing pulses played alternately along 0° and 90° in the rotating frame (see text), plotted for starting initial signal phases of 0°, 30°, 60°, 90°, 120°, and 150°. The plots are solid lines for initial phases of 0° and 90°, short dashed lines for 30° and 60°, and long dashed lines for 120° and 150°. The respective phase from the 16 echoes in **a** and **b** are overlaid in **c** and **d** as a function of the initial starting phase. In **d**, the phases for echoes 3, 7, 11, and 15 are plotted as dashed lines.

FSE is that some spins will be near the CPMG condition and produce a nearly constant magnitude with a constant phase, while other spins will be in the non-CPMG condition, producing a severely decaying magnitude with alternating phase.

This work investigates a special case of the general quadratic relationship discussed by Le Roux (13) designed to sustain echo magnitude for all initial phases. Rather than attempting to produce a sustained echo train for a large number of echoes (for SS-FSE) over a large range of B_1 (as targeted by Le Roux), it considers the feasibility of producing a stable echo train for 16–32 echoes over a modest range of B_1. The resulting echoes are slightly more stable than what are obtained using the parameters suggested by Le Roux (13) for the initial 16 echoes.

The proposed method alternates the phase of the 180° pulse between the x′ and y′ axes, i.e. {180x − 180y − 180x − 180y …}, in the fashion of the MLEV sequence (10,11). This produces a fairly stable echo train for refocusing angles near 180°, as seen in Fig. 4a. As shown in

Fig. 4b, the echo amplitudes begin to fall off significantly for refocusing angles of 140° (or less).

The phase of these echoes must also be considered. If one multiplies every other odd echo and every other even echo (e.g., 3, 4, 7, 8, 11, 12, etc.) by −1, the phase of the odd and even echoes are opposite from each other (Fig. 4c,d), i.e.:

$$f_{odd}(x, y) = f^*_{even}(x, y). \quad [1]$$

This is expressed in the Fourier domain as:

$$F_{odd}(k_x, k_y) = F^*_{even}(-k_x, -k_y). \quad [2]$$

We can therefore alter the data from the even echoes to match that of the odd echoes by: 1) reversing the phase-encoding amplitude for these echoes during data collection, 2) reversing the data in the k-space matrix in the frequency-encoded direction after data collection, and 3)
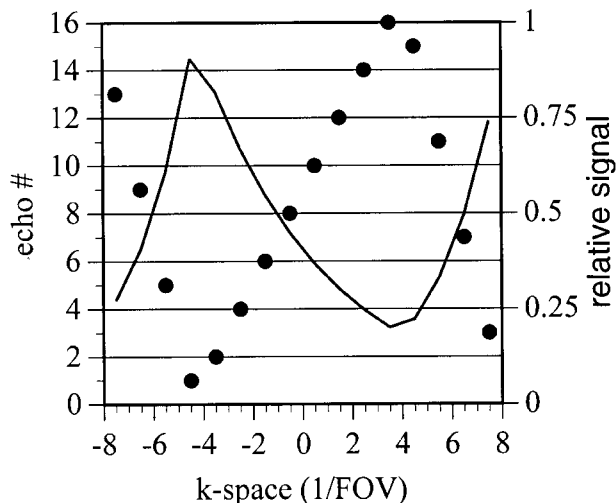
FIG. 5. An example mapping of the echoes from a 16 ETL sequence. The dots correspond to the left axis and show the actual echo-to-phase encoding mapping. The line corresponds to the right axis and illustrates the nature of T_2 decay across the width of the blade.

taking the complex conjugate of the data. In each echo train, the last two echoes are currently collected without phase-encoding to serve as reference echoes. These are necessary to line up the even and odd echoes after even echoes are reversed in time and also to correct for a global phase offset after phase conjugation of the even echoes.

The constant phase offset assumed for this work is true only when using a transmit–receive coil. When using a separate receive coil, this phase offset may vary spatially due to the difference in phase between the receive and transmit coil. If the spatial variance is too great, the odd and even echoes may have to be phase-encoded as two separate images, which can be added together afterwards

as a '2 NEX' acquisition. This has the disadvantage of doubling the minimum scan time, as well as reducing the width of the blade, which has negative consequences for the phase correction discussed below.

Finally, one should consider the mapping from echo to phase encoding used for this method. The mapping used for this work is illustrated in Fig. 5. Since the even echoes exhibit the most stable signal, they are put in the center of k-space. The odd echoes are split, with the 'first' and 'third' echoes of each group of four put on the bottom and top of the blade, respectively. These echoes are ordered to match T_2 decay at the borders with the even echoes. Since the 'third' echoes are the least stable, they are ordered from the blade edge inward, so that these echoes contribute less to the signal (due to T_2 decay) as they approach the center of k-space. The reversed order of the 'first' echoes compensates in part for this T_2 decay.

The effects of the phase correction discussed in the next section, together with the formation of the final image using only the 'real' data, rather than using the data magnitude, force the k-space data to be Hermetian symmetric across each blade. This greatly reduces any T_2-weighting of the blade which might otherwise result in blurring or similar image artifact. Finally, the combination of all of the rotated blades averages any residual T_2-weighting in the central portion of k-space, further mitigating T_2-related artifacts.

Image-Space Phase Correction

The algorithm used for image-space phase correction is illustrated in Fig. 6. After each blade is collected and the even lines are altered, as discussed above, one may perform a 2D FFT on that blade's data. This creates an image which is not aliased, but is significantly blurry in the phase-encoded direction (note that the phase-encoded direction varies for each blade). The great majority of the phase in this image was created by the particular motion
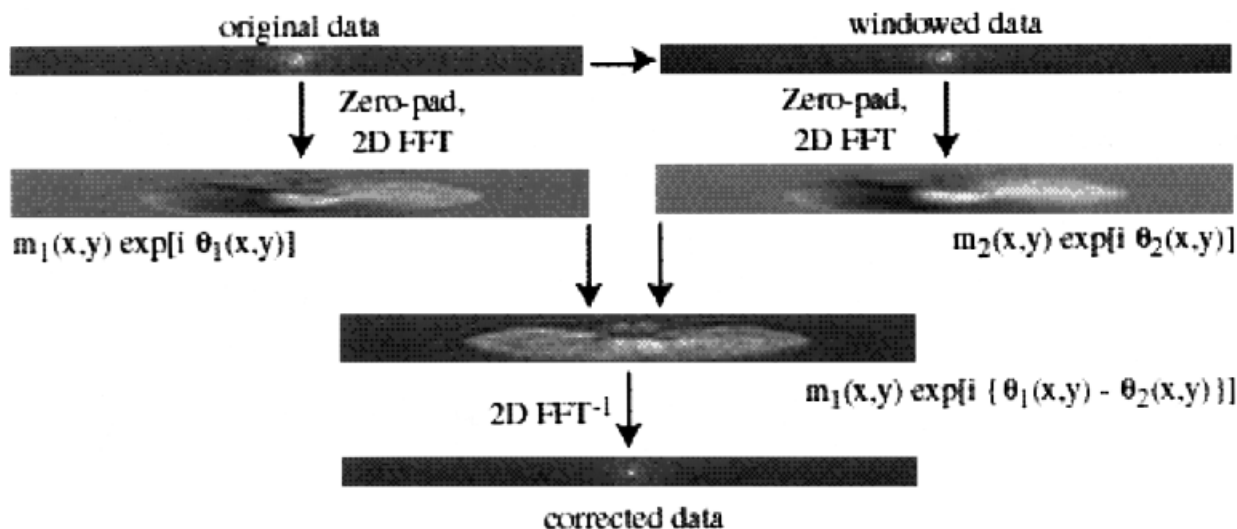

FIG. 6. Diagram of image-based phase correction performed on every blade. The original blade is windowed by a pyramidal function. Then both the original and windowed blades are zero-padded and Fourier-transformed to form images. The images' aspect ratio is kept nonuniform for computational speed. Only the real values of the complex images are shown above to indicate the degree of phase variation. The phase from the windowed dataset is then removed from the original dataset and the latter is Fourier-transformed back to create a corrected dataset.

during application of the diffusion gradients, and must be removed prior to combination of all the blades. Simply removing all phase in this image is not robust, since there is substantial Gibbs ringing in the phase-encoded direction. This in turn gives 'false' 180° phase shifts that should not be removed during the dephasing process.

To eliminate this ringing, a second copy of the blade's k-space data is multiplied by a triangular function in both frequency- and phase-encoded directions. The resulting point spread function (PSF) after the 2D FFT is $sinc^2(x)*sinc^2(y)$, which has no negative side lobes. This image has better SNR and no 'false' phase from ringing; therefore, it is considered a better candidate for phase estimation than the unwindowed image, even though the windowing process does slightly reduce the spatial resolution of the phase estimate. The phase from the second (windowed) image is removed from the first (unwindowed) image, after which the latter image is inverse Fourier-transformed to create a corrected blade. Both the windowed and unwindowed data are zero-padded prior to Fourier transformation; the reason for this is given below.

A few comments are warranted here. First, note that the corrected blade in Fig. 6 has a much more coherent echo than what is seen in the original data. This is because there is significant nonlinear phase in the image space, so image energy is dispersed in k-space. A simple linear shift of the data in k-space, as proposed for many multishot diffusion techniques to account for bulk head rotation (1), may be partially adequate when cardiac motion is quiescent, but is far from a complete correction in general.

Second, consider the requirements for doing image-based phase correction as proposed here. One must form an image from the data acquired after each application of diffusion gradients in order to apply image-based phase correction. Since, for multishot approaches, the k-space data is a subset of the complete dataset, the image will exhibit either blurring (as with PROPELLER) or aliasing (as with most multishot EPI methods, for example), depending on the chosen k-space trajectory. In the former case, the signal is combined (blurred) locally. One must therefore assume that the phase is relatively constant within this resolution limit. This is thought to be, for the most part, adequate. In the latter (aliased) case the signal is combined (aliased) over a much larger area of the imaging volume. Now one must assume that the phase of the 'properly mapped' signal at any location is the same as the phase from all aliased signal at that location, which in general is not true. Thus, for image-based phase correction, as proposed here, the data from each shot of a multishot approach must all be sufficiently sampled over some region of k-space, since the aliased signal from each shot cannot be properly corrected.

A third observation about this method is that the image-space phase correction moves data about the blade in k-space. While this is desirable in that it re-forms a coherent echo in the center of k-space (Fig. 6), it is problematic at the edge of the blade. The blades are zero-padded before Fourier transformation to image space, so that subsequent phase corrections will shift 'zeroes' into the blade rather than wrap data from one side of the blade to the other. As a result, the data at the edges of each blade are not as accurate as what is contained in the middle of the blade.

This inherent error is mitigated in the data-weighting procedure, outlined in the next section.

Correlation Weighting

After all blades have been phase-corrected as discussed above, one final correction is imposed prior to image formation. There are instances in which the phase from bulk motion during the diffusion gradient application cannot be corrected. This includes the formation of phase twists through the slice, large linear phase twists which move the majority of the signal outside of the blade, and phase shifts which vary too rapidly in image space to be adequately estimated and removed. As a result, some of the blades contain data that are more corrupted than others. These data can be removed to some extent in the data-weighting procedure. This is because, in regions of oversampling (e.g., the center of k-space), data from different blades need not be weighted evenly, and a solution can be found that gives uniform overall k-space weighting, yet weights overlapping measurements preferentially.

To assess the degree of data corruption, one may consider only the central circle in k-space, which is sampled by all blades, and correlate the data between all blades. If the above corrections worked perfectly, the individual blades should be highly correlated. But, as seen in Fig. 7b, often a small number of the blades produce images that are corrupted in some manner. By averaging all of the datasets together, one can form a reference image and the individual datasets can be correlated with that reference set. The correlation χ_i between the ith blade f_i and the reference set r is calculated as:

$$\chi_i = \frac{\left| \iint f_i(x, y)r^*(x, y) \, dx \, dy \right|}{\sqrt{\left[\iint f_i(x, y)f_i^*(x, y) \, dx \, dy \right]\left[\iint r(x, y)r^*(x, y) \, dx \, dy \right]}}.$$

[3]

The value of χ_i lies between zero and one. By Parseval's theorem, this correlation can be calculated equally well in either k-space or image space.

Once each blade has been assigned a correlation value, this can be used to calculate a relative weight, or priority, for that data. This relative weight can be incorporated into the sampling density correction using the method outlined previously (16,17). If one defines $W(k_x, k_y)$ as a set of weighted delta functions (each delta function indicating a sampling location), the referenced method finds the weighting function by solving the iterative equation:

$$W(k_x, k_y)_{i+1} = \frac{W(k_x, k_y)_i}{W(k_x, k_y)_i \otimes C(k_x, k_y)},$$ [4]

where C is a well-chosen convolution function, and $\otimes$ is the convolution operator. The iteration is started with W_0 equal to the assigned relative priority. This method forces unity weighting wherever k-space is measured. Wherever k-space is oversampled, the data from different blades are weighted according to their relative priority. In this way, bad data can be effectively removed from the center of
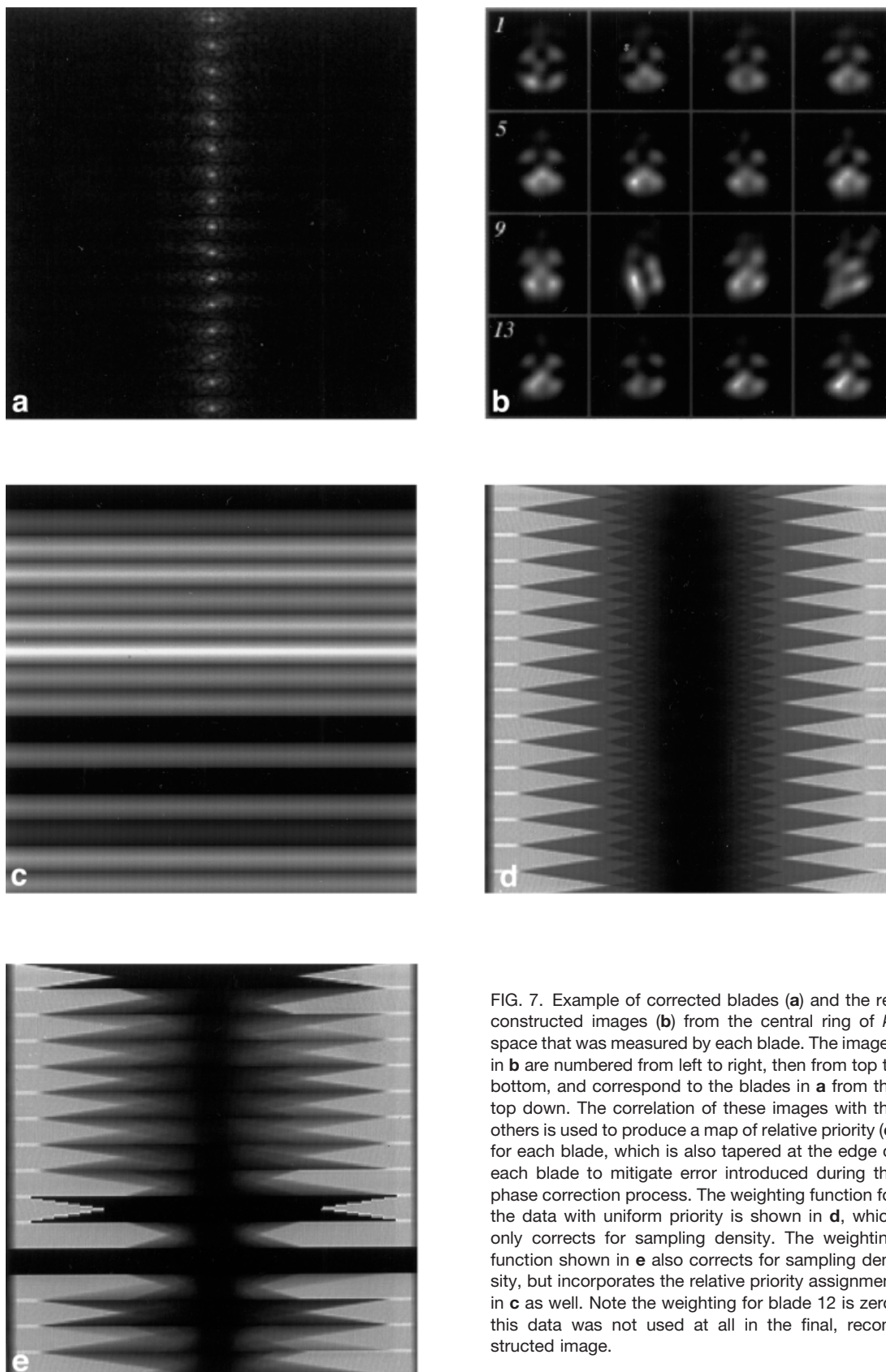
FIG. 7. Example of corrected blades (**a**) and the reconstructed images (**b**) from the central ring of *k*-space that was measured by each blade. The images in **b** are numbered from left to right, then from top to bottom, and correspond to the blades in **a** from the top down. The correlation of these images with the others is used to produce a map of relative priority (**c**) for each blade, which is also tapered at the edge of each blade to mitigate error introduced during the phase correction process. The weighting function for the data with uniform priority is shown in **d**, which only corrects for sampling density. The weighting function shown in **e** also corrects for sampling density, but incorporates the relative priority assignment in **c** as well. Note the weighting for blade 12 is zero; this data was not used at all in the final, reconstructed image.

k-space (by assigning, say, a relative priority of 0.0001 for bad data and 1.0 for good data), but can still be used at the periphery of *k*-space if desired, since it is the only data available.

For this work, the relative priority Ω_i for the data in each blade is assigned using the equation:

$$\Omega_i = \left(\frac{\chi_i - 0.92}{0.08}\right)^5, \quad 0.92 < \chi < 1$$

$$= 0, \quad 0 < \chi < 0.92. \qquad [5]$$

Equation [5] is a bit ad-hoc, but has two important features. First, data with poor correlation (i.e., below 0.92) are not used anywhere; zero-filling the area of *k*-space where it is the only measured data can visually produce less artifact than leaving these data in. Second, raising the term in parenthesis to the fifth power creates large differences in the relative weighting of well-correlated data and poorly (but still acceptable) correlated data, effectively throwing the latter out in the center of *k*-space, where it overlaps with better correlated data. The image quality does not depend significantly on the choice of the values in Eq. [5] (0.92 and 5); these numbers were arrived at over time, after visual inspection of many images. Since there are many PROPELLER blades crossing through the center of *k*-space (typically at least 12), several blades can be removed in the center of *k*-space if needed. Figure 7e illustrates the weighting based on such a correlation.

Note in Fig. 7c that the relative data priority for each blade is tapered at the edges prior to initiating the sampling density calculation. This reduces the contribution of the blade edges to the signal in the middle of *k*-space, mitigating the phase-correction artifact discussed above.

IMPLEMENTATION

Although this method can be implemented in a variety of ways, two applications are discussed here: rapid DWI imaging, and higher resolution diffusion tensor imaging (DTI). Cardiac gating was not used for any application. Fat saturation was used for all applications. It was found early on that occasional streak artifacts appeared around the scalp. This seems likely because the bright signal from the scalp, which doesn't move, lies next to brain, which moves with cardiac pulsations; this produces a spatially rapidly varying phase, which cannot be corrected by this method. Saturating the fat signal removed these artifacts. The reconstruction was fully automated, so that images were reconstructed on the scanner's host computer (SGI Octane) and automatically inserted into the scanners' image database.

Rapid Diffusion-Weighted Imaging

PROPELLER DWI was implemented on three MRI GE 1.5 T scanners (NV/i, Echospeed, and Hispeed) for imaging patients with suspected acute stroke. The parameters for clinical DWI scanning were a 107 diameter matrix over a 24 cm FOV, 5 mm thick slices (with a 2.5 mm gap), ETL = 16, TR/TE = 3300/103 msec (for NV/i). Collection of a b =

0, and three b = 1000 s/mm² images (x,y,z) took 2 min. This was designed to have similar resolution to the EPI scans we perform clinically, so that the impact of PROPELLER vs. EPI could be analyzed separately from the impact of resolution on image quality.

High-Resolution Diffusion Tensor Imaging (18)

PROPELLER DTI was implemented on a GE 1.5 T NV/i scanner and used to image a normal volunteer. The parameters were a 256 diameter matrix over a 24 cm FOV, 5 mm thick slices (with a 2.5 mm gap), ETL = 16, TR/TE = 3700/115 msec. Collection of a b = 0, and six b = 1000 s/mm² images took 10.5 min. Diffusion directions were chosen using the vectors denoting the midpoints of the edges of a cube (19), i.e., [(1,0,1), (0,1,1), (-1,0,1), (1,1,0), (-1,1,0), (0,1,-1)]. This scan was repeated four times, so that the average could simulate the SNR available at 3 T, and the standard deviation could be used to demonstrate the repeatability of this method.

RESULTS

Rapid Diffusion-Weighted Imaging

Samples of the initial results are given in Figs. 8 and 9. The images in Fig. 8 reflect early clinical results during refinement of the protocol given above and were collected at a higher resolution (170 diameter matrix). They are included because they are good examples of the immunity of PROPELLER to the metal artifact seen in EPI. This artifact masked the infarcted tissue in Fig. 8a and made the images in the lower brain completely unreadable in Fig. 8c, while the corresponding PROPELLER images were both diagnostic. The images in Fig. 9 were collected using the parameters given above. In both cases the signal pile-up artifact masked the presence of infarcts to some degree. These are initial findings from the collection of a larger number of patients; more results will be reported later as the results of a clinical study. In regions of homogeneous B_0, the PROPELLER images have similar contrast to that of EPI. In regions near significant susceptibility-induced field gradients (e.g., skull base, temporal lobes), PROPELLER DWI consistently exhibits far superior image quality, lacking the geometric warping and bright-signal artifacts common to EPI. Also, near metallic implants and nonremovable dental work the PROPELLER scans are far more robust. This robustness is due to the fact that this is an FSE-based sequence.

High-Resolution Diffusion Tensor Imaging

The mean and SD of the four sets of images from three representative slices are shown in Fig. 10. The high SD in the CSF and vitreous for the b = 0 images is due to pulsation and eye movement; when this signal is removed by application of diffusion gradients, the remaining deviation between images is near the level of the noise. Some of the remaining deviation may also be attributed to head motion of the volunteer between the scans, which lasted a total of 45 min.

Figure 11 shows the b = 0, fractional anisotropy (20), and trace diffusion images from the three representative slices in Fig. 9, all created using the averaged data. An-
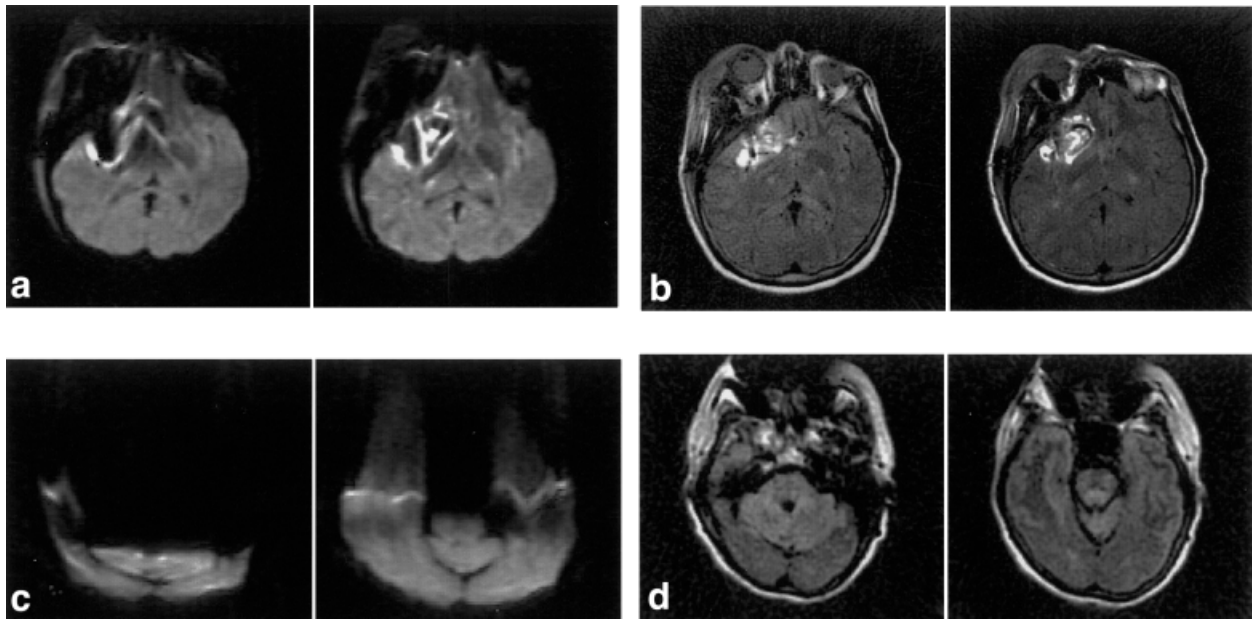
FIG. 8. Pairs of diffusion-weighted (b = 1000 s/mm^2) images using single-shot EPI (**a,c**) and PROPELLER (**b,d**) at the same slice locations for a patient who woke up symptomatic after an aneurysm clipping procedure (**a,b**) and for a patient with nonremovable dental braces (**c,d**). All images are isotropically weighted images formed from three anisotropically weighted (x, y, and z) images. These are early images, collected during the refinement of the PROPELLER DWI protocol.

other significant benefit of PROPELLER is its immunity to image warping from eddy currents. This warping is a challenge in EPI-based methods, since pixels in different regions of the head are warped in a manner that depends on the direction of the diffusion gradient, making image combination problematic. In PROPELLER imaging, however, images corresponding to different diffusion gradient directions are very well registered.
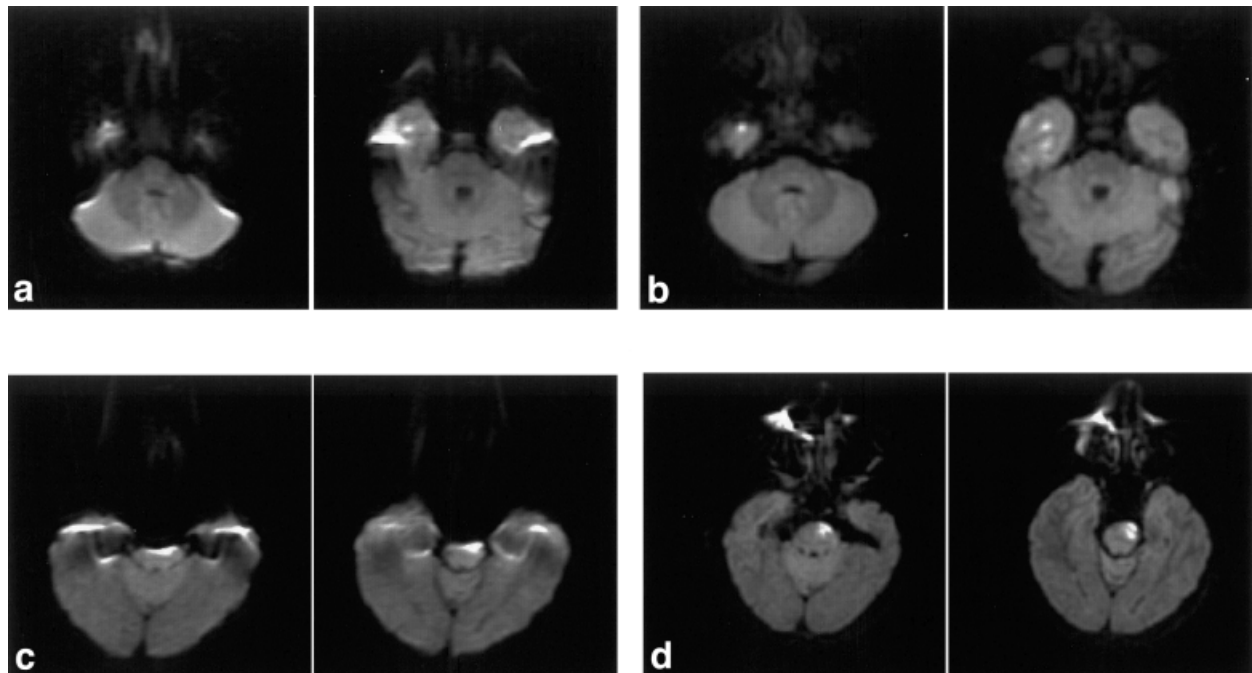

FIG. 9. Pairs of diffusion-weighted (b = 1000 s/mm^2) images using single-shot EPI (**a,c**) and PROPELLER (**b,d**) at the same slice locations for a patient with temporal lobe infarcts (**a,b**) and a patient with an infarct in the pons (**c,d**). The second patient (**c,d**) had nonremovable dental work, producing increased artifact in **c** and poor anterior fat saturation in **d**. All images are isotropically weighted images formed from three anisotropically weighted (x, y, and z) images. These images are initial images from the start of a clinical comparison between EPI and PROPELLER and were collected using the parameters in the text.
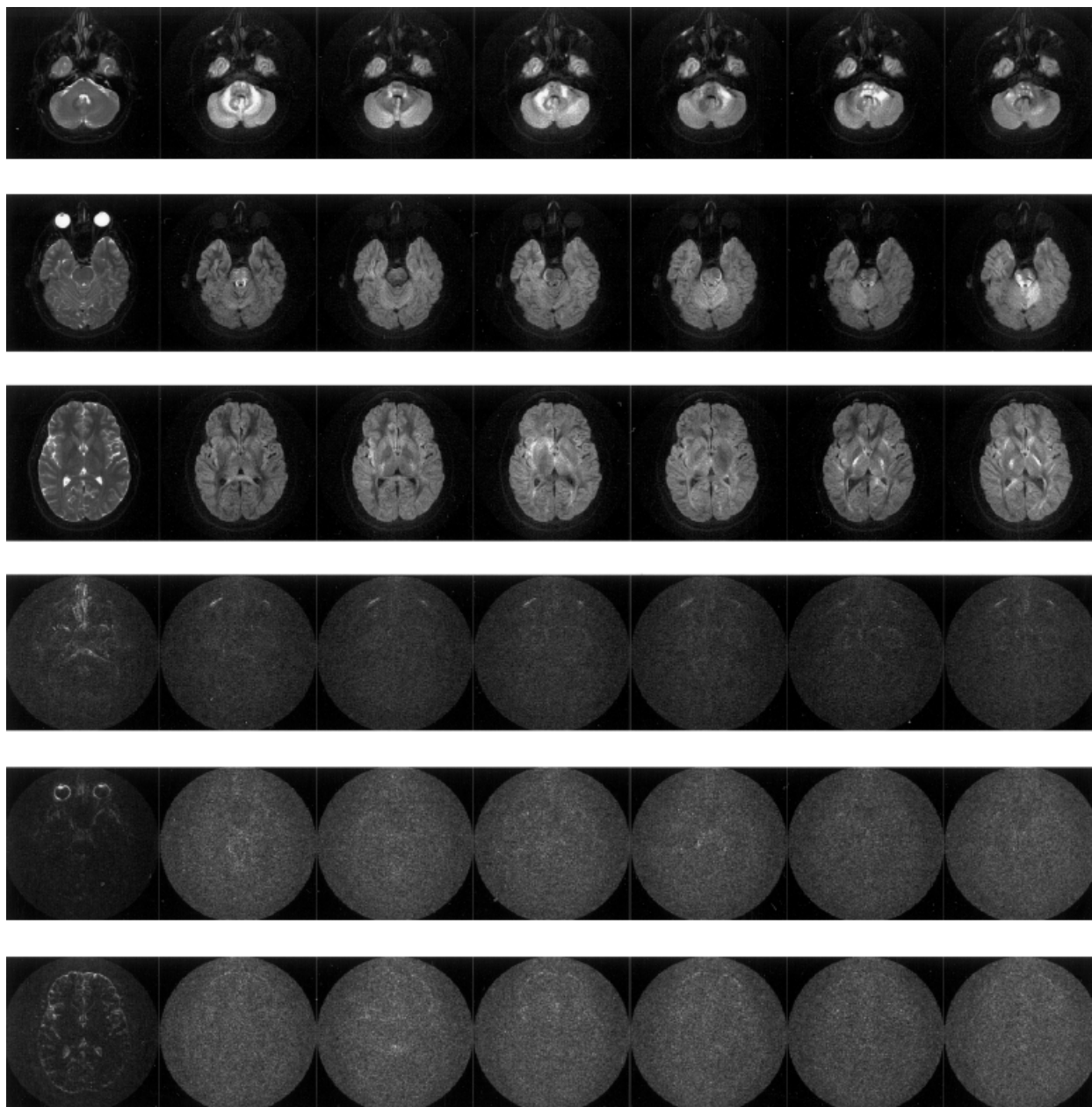
FIG. 10. Average (top three rows) and standard deviation (bottom three rows) of four DTI acquisitions, from three representative slices. For all rows, the b = 0 image dataset is on the left, followed by the six b = 1000 s/mm^2 images. The diagonal directions for columns 2–7 correspond to (AS↔PI, PS↔AI, RI↔LS, RS↔LI, AR↔PL, AL↔PR), where A/P = Anterior/Posterior, S/I = Superior/Inferior, and L/R = volunteer's Left/Right. More details are given in the text.

DISCUSSION

The proposed method has the primary benefit of greatly reduced sensitivity to magnetic field inhomogeneities. This eliminates the signal pile-up artifact seen in single-shot EPI DWI, which has the potential to mask pathology. It is also much more feasible to acquire high-resolution DWI than with single-shot EPI imaging. The sequence is virtually immune to image warping due to eddy currents. There is a 50% increase in minimum imaging time over conventional FSE due to the oversampling in the center of k-space. This ordinarily would result in increased SNR;

however, the nonuniform data weighting diminishes some of this SNR return.

It is likely that the slice profiles for PROPELLER diffusion scans are compromised (narrowed) at the edges, where the refocusing pulse falls off from 180°. Here the phase shifting algorithm is less effective and the signal will fall off significantly (see Fig. 4b). This will not only decrease the available signal, but may also add some 'noise' (signal variability, really) to the image, since the signal dropout will be motion-dependent. This was mitigated somewhat by extending the refocusing slab profile
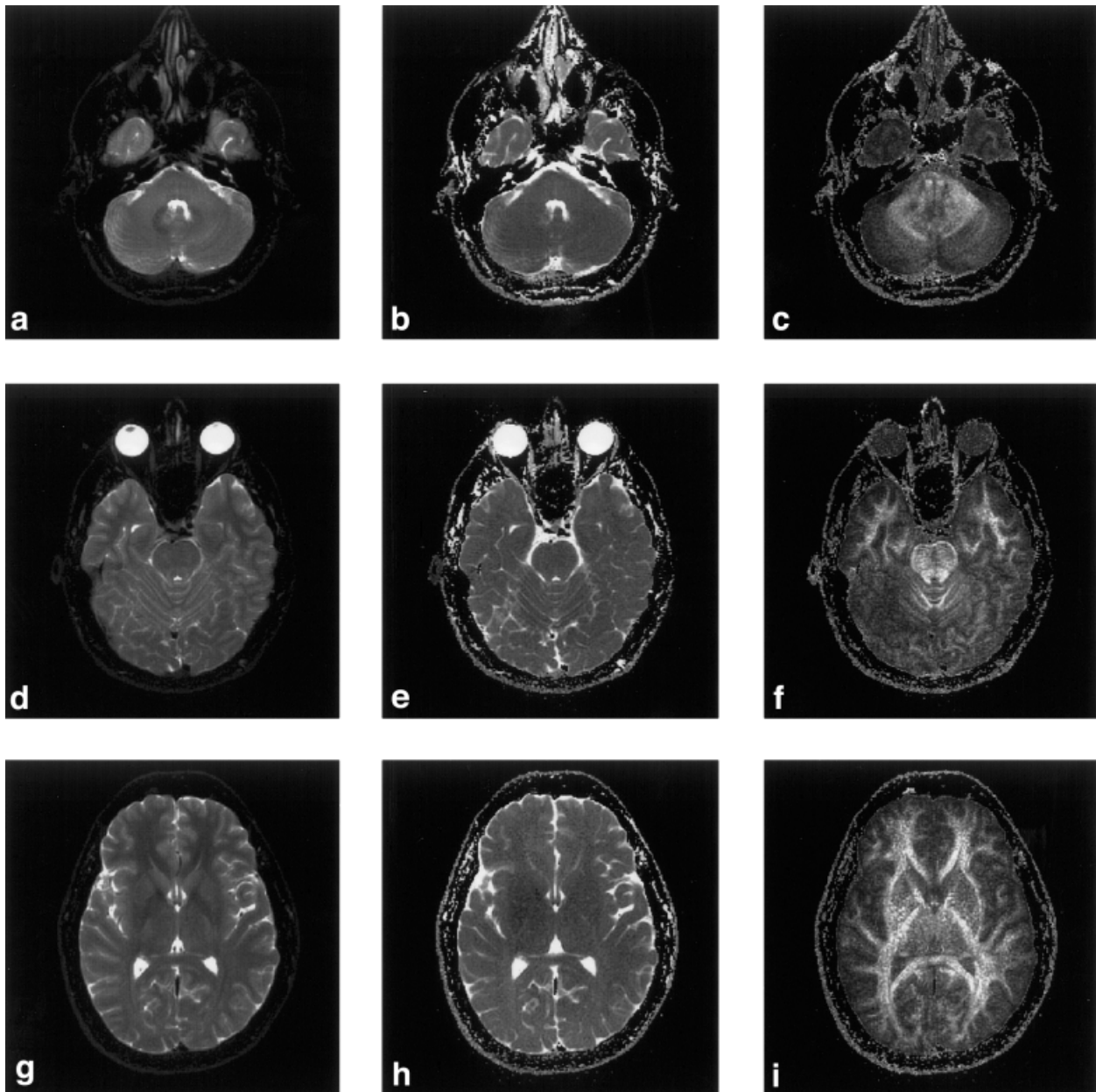
FIG. 11. The b = 0 (**a,d,g**), trace diffusion (**b,e,h**), and fractional anisotropy (**c,f,i**) images from the three slices in Fig. 9.

beyond the excitation slice profile a bit, so that more of the excited slice receives a refocusing angle near 180°. Simple SNR measurements suggest that this effect is not significant; however, studying this signal loss and refining the refocusing pulse is an area for possible improvement in the future.

It was noted in the Image-Space Phase Correction section that the proposed phase correction algorithm requires that the data from each shot (TR) be 'sufficiently sampled,' i.e., produces only blurring and not aliasing in the corresponding image. If one combines this requirement with the desire that the data from each shot are self-navigated (measure the center of k-space), there are few trajectory sets other than PROPELLER blades that are adequate. For example, variable density spiral methods (21), which were

investigated by us for this application early on, are not in general robust due to the aliased high spatial frequencies in each shot. One could collect the PROPELLER blade using an EPI approach and eliminate the CPMG problem. However, since the k-space trajectory is filled at the same speed as single-shot EPI in the phase encode direction, data are warped for a single blade by the same amount as for a single-shot method. When multiple blades are combined, this 'n-pixel' warping turns into a blurring with a radius of n pixels, which severely compromises image quality.

Another potential benefit of the PROPELLER method of data collection is that additional motion correction (in-plane rotation, translation) is possible for uncooperative patients. To date, this has proven to be difficult to imple-

ment robustly due to the instability of the data in the central region of *k*-space. Finally, the radial nature of the PROPELLER trajectory is helpful, in that any remaining artifacts tend to be spread in a benign manner, similar to projection reconstruction.

ACKNOWLEDGMENTS

REFERENCES

1. Anderson AW, Gore JC. Analysis and correction of motion artifacts in diffusion weighted imaging. Magn Reson Med 1994;32:379−387.
2. Ordidge RJ, Helpern JA, Qing ZX, Knight RA, Nagesh V. Correction of motional artifacts in diffusion-weighted MR images using navigator echoes. Magn Reson Imag 1994;12:455−460.
3. de Crespigny AJ, Marks MP, Enzmann DR, Moseley ME. Navigated diffusion imaging of normal and ischemic human brain. Magn Reson Med 1995;33:720−728.
4. Butts K, de Crespigny A, Pauly JM, Moseley M. Diffusion-weighted interleaved echo-planar imaging with a pair of orthogonal navigator echoes. Magn Reson Med 1996;35:763−770.
5. Trouard TP, Theilmann RJ, Altbach MI, Gmitro AF. High-resolution diffusion imaging with DIFRAD-FSE (diffusion-weighted radial acquisition of data with fast spin-echo) MRI. Magn Reson Med 1999;42:11−18.
6. Norris DG, Bornert P, Reese T, Leibfritz D. On the application of ultra-fast RARE experiments. Magn Reson Med 1992;27:142−164.
7. Schick F. SPLICE: sub-second diffusion-sensitive MR imaging using a modified fast spin-echo acquisition mode. Magn Reson Med 1997;38:638−644.
8. Alsop DC. Phase insensitive preparation of single-shot RARE: application to diffusion imaging in humans. Magn Reson Med 1997;38:527−533.
9. Mori S, van Zijl PC. A motion correction scheme by twin-echo navigation for diffusion-weighted magnetic resonance imaging with multiple RF echo acquisition. Magn Reson Med 1998;40:511−516.
10. Shaka A, Rucker S, Pines A. Iterative Carr-Purcell trains. J Magn Reson 1988;77:606−611.
11. Guillion T. New, compensated Carr-Purcell sequences. J Magn Reson 1990;89:479−484.
12. Bastin ME, Le Roux P. Application of non-CPMG fast-spin-echo sequences to MR diffusion imaging. In: Proceedings of the 9th Annual Scientific Meeting and Exhibition, ISMRM, Glasgow, 2001.
13. Le Roux P. Spin echoes with a quadratic phase modulation of the RF pulse train. In: Proceedings of the 9th Annual Scientific Meeting and Exhibition, ISMRM, Glasgow, 2001.
14. Murdoch JB. An "effective" method for generating spin-echo intensity expressions. In: Proceedings of the 2nd Annual Scientific Meeting, SMR, San Francisco, 1994.
15. Pipe JG. Motion correction with PROPELLER MRI: application to head motion and free-breathing cardiac imaging. Magn Reson Med 1999;42:963−969.
16. Pipe JG, Menon P. Sampling density compensation in MRI: rationale and an iterative numerical solution. Magn Reson Med 1999;41:179−186.
17. Pipe JG. Reconstructing MR images from undersampled data: data-weighting considerations. Magn Reson Med 2000;43:867−875.
18. Basser PJ. Inferring microstructural features and the physiological state of tissues from diffusion-weighted images. NMR Biomed 1995;8:333−344.
19. Basser PJ, Pierpaoli C. A simplified method to measure the diffusion tensor from seven MR images. Magn Reson Med 1998;39:928−934.
20. Pierpaoli C, Basser PJ. Toward a quantitative assessment of diffusion anisotropy. Magn Reson Med 1996;36:893−906.
21. Tsai CM, Nishimura DG. Reduced aliasing artifacts using variable-density *k*-space sampling trajectories. Magn Reson Med 2000;43:452−458.